



Automatic multi-resolution shape modeling of multi-organ structures

Juan J. Cerrolaza ^{a,*}, Mauricio Reyes ^b, Ronald M. Summers ^c,
Miguel Ángel González-Ballester ^d, Marius George Linguraru ^{a,e}

^a Sheikh Zayed Institute for Pediatric Surgical Innovation Children's National Health System, Washington DC 20009, USA

^b Surgical Technology and Biomechanics Department, University of Bern, Bern, Switzerland

^c Department of Radiology and Imaging Sciences, National Institutes of Health Clinical Center, Bethesda, MD 20814, USA

^d ICREA, and Universitat Pompeu Fabra, Barcelona, Spain

^e School of Medicine and Health Sciences, George Washington University, Washington DC, USA

ARTICLE INFO

Article history:

Received 13 November 2014

Revised 2 April 2015

Accepted 9 April 2015

Available online xxx

Keywords:

Point distribution model (PDM)

Multi-resolution

Hierarchical modeling

Statistical shape model

Active shape model

ABSTRACT

Point Distribution Models (PDM) are among the most popular shape description techniques and their usefulness has been demonstrated in a wide variety of medical imaging applications. However, to adequately characterize the underlying modeled population it is essential to have a representative number of training samples, which is not always possible. This problem is especially relevant as the complexity of the modeled structure increases, being the modeling of ensembles of multiple 3D organs one of the most challenging cases. In this paper, we introduce a new GEneralized Multi-resolution PDM (GEM-PDM) in the context of multi-organ analysis able to efficiently characterize the different inter-object relations, as well as the particular locality of each object separately. Importantly, unlike previous approaches, the configuration of the algorithm is automated thanks to a new agglomerative landmark clustering method proposed here, which equally allows us to identify smaller anatomically significant regions within organs. The significant advantage of the GEM-PDM method over two previous approaches (PDM and hierarchical PDM) in terms of shape modeling accuracy and robustness to noise, has been successfully verified for two different databases of sets of multiple organs: six subcortical brain structures, and seven abdominal organs. Finally, we propose the integration of the new shape modeling framework into an active shape-model-based segmentation algorithm. The resulting algorithm, named GEMA, provides a better overall performance than the two classical approaches tested, ASM, and hierarchical ASM, when applied to the segmentation of 3D brain MRI.

© 2015 Elsevier B.V. All rights reserved.

1. Introduction

The segmentation and shape analysis of human organs is of crucial importance to better design tools for diagnosis and treatment, study diseases, and perform patient follow-up (Heimann and Meinzer, 2009). Due to the inherent limitations of traditional bottom-up segmentation methods based solely on pixel-level information, the analysis of organs in 3D radiological data calls for shape description methods capable of dealing with the high variability and complexity of the human anatomy, and the presence of image inaccuracies (e.g., partial volume effects (González-Ballester et al., 2002),

occlusions, image noise, or low contrast), as it is often the case of medical images.

Several statistical shape models, such as deformable templates (Grenander et al., 1991) or spherical harmonic descriptors (Kelemen et al., 1998), emerged at the end of the last century. The Point Distribution Model (PDM) proposed by Cootes et al. (1995) has been of considerable research interest since its inception in the early 1990s, and its versatility and relative simplicity facilitated the emergence of a large number of extensions of the original framework (Cootes et al., 1994; Duta and Sonka, 1998; Hamarneh and Gustavsson, 2004; Rajamani et al., 2007). Traditionally, medical imaging and statistical shape models have focused on single-organ applications. However, aware of the importance of shifting from organ-based to organism-based approaches, there has been growing interest in the development of more comprehensive models in recent years (Linguraru et al., 2012; Okada et al., 2008). An interesting property of PDMs is their inherent capacity to model multi-object structures by concatenating the descriptors of all the objects and performing global statistics on the resulting tuple. However, two major drawbacks limit its

* Corresponding author at: Sheikh Zayed Institute for Pediatric Surgical Innovation Children's National Health, 1615 Q St NW, Apt. 201, Washington, DC 20009, USA. Tel.: +1 202 5944 587.

E-mail addresses: jcerrola@cnmc.org, jjcerromar@gmail.com (J.J. Cerrolaza), mauricio.reyes@istb.unibe.ch (M. Reyes), rms@nih.gov (R.M. Summers), ma.gonzalez@upf.edu (M.Á. González-Ballester), mlingura@cnmc.org (M.G. Linguraru).

utility when working with structures of increased complexity. First, PDMs do not respect object-based scale levels, lacking the ability to explicitly describe important local geometric information, such as locality or inter-organ relations. Second, the models typically face the high-dimension-low-sample-size (HDLSS) problem, which appears when the number of parameters needed to accurately describe the geometry is larger than the number of training samples available, as it is the case in many medical imaging applications.

Trying to overcome the shortcomings of PDMs, some authors have proposed interesting versions of the classical PDM, exploiting the possibilities of incorporating multi-resolution hierarchical analysis into shape modeling. [Davatzikos et al. \(2003\)](#) proposed a hierarchical decomposition of shape into small pieces of information via the wavelet transform. However, whereas the independent modeling of these bands allows reducing the dimensionality of the problem, and thus the HDLSS effect, it also reduces the robustness of the model as shown by [Cerrolaza et al. \(2012\)](#). An interesting attempt to describe the interrelations between objects at different scales statistically is the multi-scale framework proposed by [Lu et al. \(2007\)](#) using m-reps as the geometric representation of shapes. In spite of the valuable multi-scale properties of m-reps, they are less intuitive than the landmark-based representation used in PDMs, which is probably one of the simplest and most generic methods used to represent shapes. The inter-organ relation is also integrated into the framework presented by [Okada et al. \(2013\)](#), where the spatial correlations among organs were encoded into a correlation graph. This information was used to define the sequential segmentation of multiple organs in abdominal Computer Tomography (CT) images. The aim of this hierarchical approach was to improve the accuracy in segmenting more challenging abdominal organs, such as the gallbladder and pancreas, relying on the available segmentation of more stable organs surrounding them. However, the errors in the segmentation of the stable organs are also propagated, and thus affecting the subsequent predictions and segmentations due to the proposed sequential formulation. Inter-organ relations were also incorporated in the method proposed by [Suzuki et al. \(2012\)](#), whose atlas-based multi-organ segmentation approach was able to automatically handle missing organs due to surgical resection. In our previous work ([Cerrolaza et al., 2012](#)), we proposed a new multi-resolution hierarchical variant of PDM (MRH-PDM), able to efficiently characterize inter-object relations, as well as the particular locality of each object separately. Even though the potential of MRH-PDM was successfully verified in terms of accuracy and robustness, the absence of an automatic grouping approach can hinder its practical application when working with complex data with a large number of objects. Another important limitation of MRH-PDM was the limited capability to model the intra-object variability of complex organs, considering the single objects as the simplest structures to model at the finest resolution level (i.e., each object modeled separately).

In this paper, we present a new GEneralized Multi-resolution PDM (GEM-PDM) to address the above limitations of MRH-PDM: intra-object analysis, and automatic multi-resolution hierarchical decomposition. Extending the original hierarchical modeling of PDM introduced in [Cerrolaza et al. \(2012\)](#) to sub-parts of single-object structures leads to a more versatile and generalizable multi-organ-, organ- and sub-organ-based framework, able to model efficiently both, the inter- and intra-organ variability. The configuration of the algorithm is built around a new agglomerative landmark clustering approach, which provides an automatic hierarchical decomposition of the multi-organ structure under study. A first version of the framework described here was recently presented in [Cerrolaza et al. \(2014\)](#), showing the potential of GEM-PDM for the statistical modeling of 3D subcortical structures. In the present work, we provide an additional and detailed description of the method and conduct new tests that allow us to better characterize the performance of the algorithm, and its value for segmentation. In particular the behavior of GEM-PDM is evaluated in

terms of shape modeling accuracy and noise robustness, and compared with two popular alternatives, the classical PDM ([Cootes et al., 1995](#)) and the original hierarchical PDM ([Davatzikos et al., 2003](#)), using two different datasets for our experiments: sets of six brain subcortical structures and groups of seven abdominal organs. Finally, we also analyze the performance of the new shape modeling framework when it is integrated into a new segmentation algorithm, termed here GEneralized Multi-resolution Active shape model (GEMA).

2. Multi-resolution decomposition of 3D structures

In this section, we introduce the concept of multi-resolution decomposition of 3D structures, which is one of the cornerstones of the new GEM-PDM presented in [Section 3](#). Wavelet-based multi-resolution decomposition will allow us to efficiently model the inter-object relations and the local variations of each particular organ in a complex multi-object structure. For a detailed description of multi-resolution analysis theory the reader is referred to the works presented by [Finkelstein and Salesin \(1994\)](#); [Lounsherry et al. \(1997\)](#); [Stollnitz et al. \(1996\)](#) for further information.

Let \mathbf{x} be the vector form of a 3D shape defined by the concatenation of the three coordinates of the $K \in \mathbb{N}$ landmarks used to describe the structure. In the most general case of a multi-object shape composed of $M \in \mathbb{N}$ single-object structures, the vector form is $\mathbf{x} = (\mathbf{x}_1; \dots; \mathbf{x}_M)^T$, where \mathbf{x}_j ($1 \leq j \leq M$) represents the j th object. Using the multi-object generalization ([Cerrolaza et al., 2012](#)) of the matrix notation initially proposed by [Lounsherry et al. \(1997\)](#), the multi-resolution analysis of \mathbf{x} can be formulated as

$$\mathbf{x}^r = \mathbf{A}^r \mathbf{x}^{r-1} \quad (1)$$

$$\mathbf{z}^r = \mathbf{B}^r \mathbf{x}^{r-1}, \quad (2)$$

where \mathbf{A}^r and \mathbf{B}^r represent the analysis filters, and $r \in \mathbb{N}$ indicates the level of resolution, with $r = 0$ being the finest one (i.e., $\mathbf{x}^0 = \mathbf{x}$). Equation (1) implements the filtering and downsampling of \mathbf{x}^{r-1} , providing a lower resolution version of it, while (2) captures the lost detail between \mathbf{x}^{r-1} and \mathbf{x}^r . \mathbf{A}^r and \mathbf{B}^r must be constructed so that the original mesh can be recovered exactly from the low-resolution version, \mathbf{x}^r , and the wavelet coefficients, \mathbf{z}^r . During these complementary processes, the coarser version of the polyhedron is refined by subdividing each triangle (assuming a triangular mesh is used) into four sub-triangles by means of additional vertices at edge midpoints. The resulting refined mesh is modified according to the wavelet coefficients previously obtained. These refining and modifying steps are computed by the synthesis equation

$$\mathbf{x}^{r-1} = \mathbf{F}^r \mathbf{x}^r + \mathbf{G}^r \mathbf{z}^r, \quad (3)$$

where \mathbf{F}^r and \mathbf{G}^r represent the synthesis filters. In the work of [Lounsherry et al. \(1997\)](#), the authors describe a multi-resolution framework to obtain the analysis and synthesis filters for arbitrary topological surfaces. Since all the organs considered in this paper have spherical topology, we define the multi-resolution domain using the octahedron as the reference mesh, with a 4-to-1 splitting step. The wavelet transform was implemented using the lifting scheme and a butterfly predictor, as explained by [Schroder and Sweldens \(1995\)](#). The method proposed by [Praun and Hoppe \(2003\)](#) is employed to parameterize each structure onto an octahedron. [Fig. 1](#) depicts the multi-resolution decomposition of a multi-organ shape composed by six subcortical structures.

3. Generalized multi-resolution hierarchical PDM

With the method described in [Section 2](#), it is possible to decompose a multi-object structure into different levels of resolution, which allows us to create specific statistical shape models characterizing

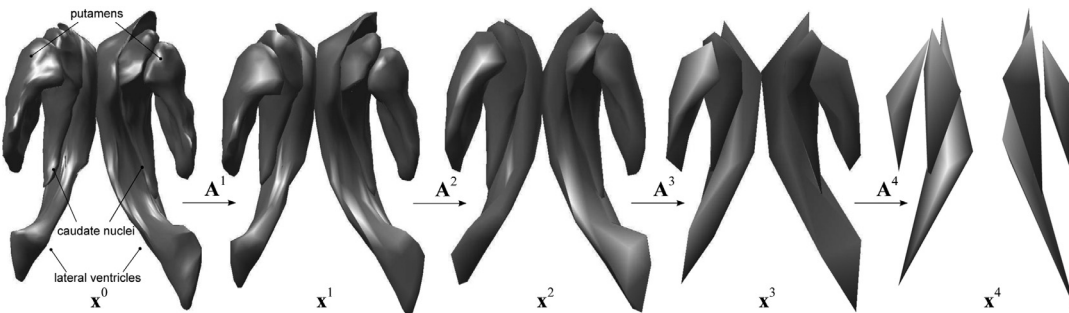


Fig. 1. Example of the multi-resolution decomposition of a multi-object shape. From left to right, fine-to-coarse representations of six subcortical brain structures as they are processed by the wavelet analysis filter, \mathbf{A} .

different inter-object associations at each scale. Thus, the particulars of each single object/organ can be modeled individually at the finest resolution by different PDMs (e.g., one model for each organ) (see Figs. 3(d) and 4(d)). Then, as we move toward lower levels of resolution, additional spatial restrictions can be imposed by means of more global shape models that attend to the inter-object relations not modeled in previous resolutions (Figs. 3(a)–(c) and 4(b–c)). In particular, a global statistical shape model of the whole multi-object set is built at the coarsest resolution in order to guarantee the coherent disposition of the elements (Figs. 3(a) and 4(b)).

In the original MRH-PDM formulation described by Cerrolaza et al. (2012), single organs were considered as the simplest structures to model at the finest resolution levels, which limits the capability to model the variability in subparts of a single object. Relaxing this condition, we go one step further in the development of hierarchical PDMs, introducing a general framework where any possible grouping of landmarks is considered. Whereas MRH-PDM established a specific division of the M objects into $M^r \in \mathbb{N}$ disjoint subsets at each level of resolution (i.e., only complete objects can be part of a subset), here we propose a general definition of the disjoint subsets. Thus, at each level of resolution r we define a particular division of the K^r landmarks into M^r separate clusters, $(\mathbf{S}_1^r, \dots, \mathbf{S}_{M^r}^r)$. \mathbf{S}_s^r ($s = 1, \dots, M^r$) is formed by the indices of the landmarks contained in this subset, and therefore, $\cap_{s=1}^{M^r} \mathbf{S}_s^r = \emptyset$ and $\cup_{s=1}^{M^r} \mathbf{S}_s^r = (1, \dots, K^r)$. In addition, the following condition is imposed. Suppose $\mathbf{S}_{s^r-1}^{r-1}$ (i) represents the i th element of the s^{r-1} th subset defined at the $r-1$ th resolution level, and $\widehat{\mathbf{S}}_{s^r}^r$ is the propagation of $\mathbf{S}_{s^r}^r$ to $r-1$, then

$$\mathbf{S}_{s^r-1}^{r-1}(i) \in \widehat{\mathbf{S}}_{s^r}^r \implies \forall i \mathbf{S}_{s^r-1}^{r-1}(i) \in \widehat{\mathbf{S}}_{s^r}^r \quad (4)$$

That is, two sets of landmarks that have been grouped separately at a specific level of resolution, should not be jointly modeled at finer resolutions; or equivalently, the clusters created in the r th resolution derive from the fragmentation of clusters in $r+1$ th resolution. Despite the intuitive meaning of (4), there is a challenge yet to be resolved: the propagation of the clusters between two consecutive resolutions. Let \mathbf{L}^r be a $(3K^r \times 1)$ vector (i.e., the same size as \mathbf{x}^r) containing the labels of the subset to which each landmark of \mathbf{x}^r belongs; i.e., if $\mathbf{x}^r(i) \in \mathbf{S}_s^r$ then $\mathbf{L}^r(i) = s$. With this notation, we can estimate $\widehat{\mathbf{L}}^{r-1}$, the propagation of the subdivision defined by \mathbf{L}^r to the landmarks of the following resolution, $r-1$. The estimation is done by means of the synthesis matrix, \mathbf{F}^r , i.e., $\widehat{\mathbf{L}}^{r-1} = [\mathbf{F}^r \mathbf{L}^r]_{1:M^r}^T$, where the $\lfloor \cdot \rfloor_a^b$ operator rounds to the nearest integer in the range $[a, b]$.

Once the multi-resolution configuration has been defined (process described in Section 4), it is necessary to statistically model the underlying population of each subset via PDM

$$PCA(\mathbf{S}_s^r) \rightarrow \{\bar{\mathbf{x}}_s^r, t_s^r, \mathbf{P}_s^r, \Lambda_s^r\}, \quad (5)$$

where $\bar{\mathbf{x}}_s^r$ represents the average vector of landmarks included in \mathbf{S}_s^r , and \mathbf{P}_s^r and Λ_s^r contain the t_s^r main eigenvectors, and the corresponding eigenvalues $(\lambda_{s,1}^r, \dots, \lambda_{s,t_s^r}^r)$, respectively. The integration

of GEM-PDM into a full segmentation framework is discussed in Section 5.

4. Automatic hierarchical decomposition

The number of possible hierarchical configurations can be considerably high when working with complex structures composed by multiple objects. This makes the manual definition of an appropriate configuration difficult and possibly subjective and irreproducible, as suggested in Cerrolaza et al. (2012), and limits the practical utility of the MRH-PDM. In this section we introduce a new landmark clustering approach that allows us to automatically define the division of landmarks into separate clusters at each resolution. The clustering process was initially inspired by the work presented by Roy et al. (2006), which was originally conducted for vector field segmentation of moving objects in 2D videos, and extended to 3D objects by Reyes et al. (2009) to study the anatomical variability of single organs via principal factor analysis. Here we propose a more general approach based on the agglomerative hierarchical clustering method presented by Ward (1963). Ward's approach is a general agglomerative hierarchical clustering procedure where, starting from an initial state in which all elements are considered as separate clusters, a pair of clusters is chosen to merge at each step based on the optimal value of an objective function. Here we propose the following tailored objective function:

$$J(\Omega) = \alpha_1 \int_{\Omega} \left(\frac{|\mathbf{V}_{\Omega} \times \mathbf{V}_i|}{|\mathbf{V}_i|} \right)^2 \frac{L_{\max}}{|\mathbf{V}_i|} di + \alpha_2 \left(1 - \frac{\int_{\Omega} di}{\int_{\mathbf{S}} di} \right) + \alpha_3 H(\Omega), \quad (6)$$

where α_1 , α_2 and α_3 are real values such that $\sum \alpha_i = 1$. $\Omega \subseteq \mathbf{S}$ represents a region or subdomain within the set of landmarks \mathbf{S} we want to divide into an optimal set of clusters. In the context of shape modeling, an optimal cluster of landmarks can be intuitively defined as a group of points with a similar variability pattern (i.e., deformation vector). Thus, the first component of (6) takes into account the collinearity between deformation vectors within the domain Ω , \mathbf{V}_i , and the predominant vector direction \mathbf{V}_{Ω} . The notion of dominant direction of a set of vectors was originally proposed by Rao and Schunk (1989) and exploited by Roy et al. (2006) to identify regions of vectors with a similar direction (i.e., similar variability pattern). Fig. 2 illustrates this concept graphically for a 2D example. It can be observed (see Fig. 2(c)) how the collinearity between \mathbf{V}_i and \mathbf{V}_{Ω} , defined by the term $|\mathbf{V}_{\Omega} \times \mathbf{V}_i|/|\mathbf{V}_i|$, which can be rewritten as $\sin(\theta_{\Omega,i})$ where $\theta_{\Omega,i} = \widehat{\mathbf{V}_{\Omega}}, \mathbf{V}_i$, is lower for those vectors with direction similar to \mathbf{V}_{Ω} (e.g., vectors within the region Ω). In the particular context of GEM-PDM, we define the deformation vector at landmark $\mathbf{l}_i^r \in \mathbf{S}_s^r$ ($1 \leq i \leq K^r$) as

$$\mathbf{V}_i^r = \frac{\sum_{t=1}^{t_s^r} \mathbf{P}_{s,t,i}^r \lambda_{s,t}^r}{\sum_{t=1}^{t_s^r} \lambda_{s,t}^r}, \quad (7)$$

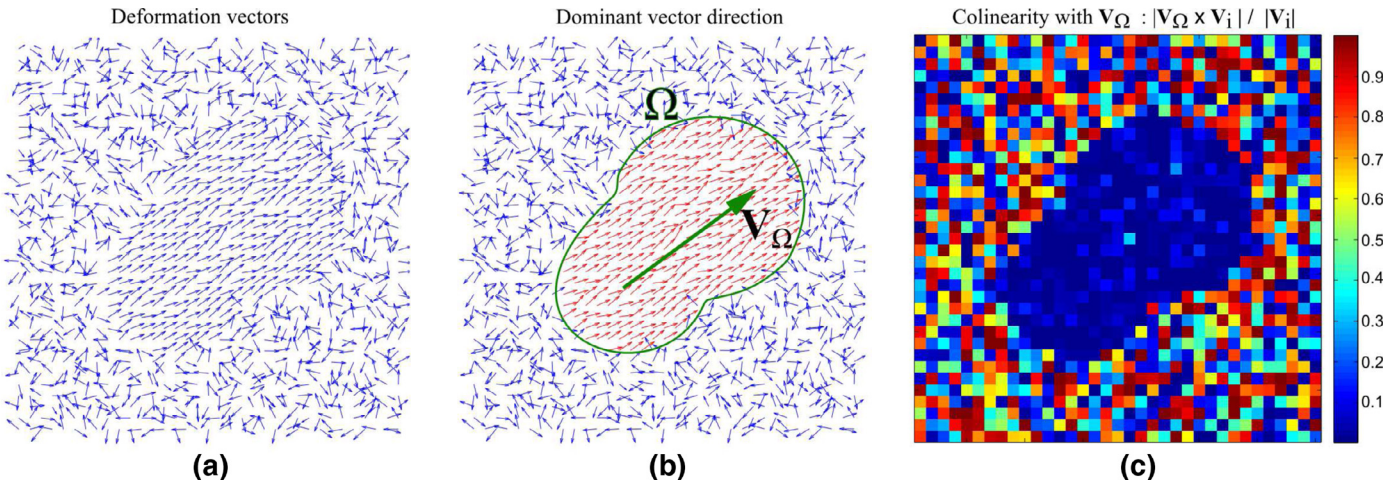


Fig. 2. Dominant vector direction and colinearity. (a) Artificially generated grid of deformation vectors. Part of the vectors were generated randomly whereas those inside the region Ω were generated from a normal distribution ($\text{std} = 0.08 \text{ rad}$). (b) Dominant vector direction \mathbf{V}_Ω within the domain Ω . (c) Colinearity between \mathbf{V}_i and \mathbf{V}_Ω : $|\mathbf{V}_\Omega \times \mathbf{V}_i| / |\mathbf{V}_i|$.

where $\mathbf{p}_{s,t,i}^r$ is the corresponding displacement vector defined by the t th eigenvector of $\text{PCA}(\mathbf{S}_s^r)$. The dominant direction $\mathbf{V}_{s,\Omega}^r$ is defined as the eigenvector associated with the highest eigenvalue of the symmetric, positive, 3×3 matrix $M_s^r(\Omega) = \int_{\Omega} \mathbf{V}_i^r (\mathbf{V}_i^r)^T di$, and $L_{s,\max}^r = \max_S \{ \|\mathbf{V}_i^r\| \mid i \in S_s^r \}$. If Ω contains landmarks with similar deformation vectors, then any vector can represent the dominant direction, and the first term in (6) is equal to zero. Even more in this case, any subset of Ω has an energy equal to zero. Since our purpose is to find the largest domain Ω containing vector with the same direction (see Fig. 2), the second term in Eq. (6) acts as a maximal area constraint to prevent the trivial solution where each landmark is grouped independently.

The aim of the third term, $H(\Omega)$, defined as the Hausdorff distance (Rockafellar and Wets, 2005) between the objects that compose Ω normalized by the maximum distance among objects in S , is to promote the grouping of objects that are spatially close. When minimizing equation (6), it is desirable that the colinearity between deformation vectors be the dominant term in the generation of clusters, while the second and third term act as additional constraints to guarantee the consistency of the final results, i.e., $\alpha_1 \gg (\alpha_2, \alpha_3)$. Starting with the coarsest resolution, $r = R$, and imposing $M^R = 1$ as additional initial condition, the hierarchical configuration of GEM-PDM is obtained by using Ward's hierarchical clustering in each subset obtained at $r + 1$.

From the family of partitions provided by Ward (1963) algorithm, we define the optimal landmark division based on a tailored version of the Silhouette coefficient (Rousseeuw, 1987) defined as follows. Suppose that landmark l_i is assigned to cluster Ω_i . Then, we define how well l_i is assigned to its cluster as $a_i = J(\Omega_i) - J(\Omega_{i \setminus l_i})$, where $\Omega_{i \setminus l_i}$ represents the cluster Ω_i after removing l_i . Thus, large a_i represents a high dissimilarity between l_i and Ω_i . In the same way, we define the dissimilarity of l_i to any other cluster Ω_j ($j \neq i$) to which l_i is not member as $b_i = \min b_{i,j}$, where $b_{i,j} = J(\Omega_{j+l_i}) - J(\Omega_j)$, and Ω_{j+l_i} represents the union of l_i and Ω_j . Constraining the values of a_i and b_i to the range $[0, 1]$ by means of the logistic function, $LF(\cdot)$, we define the Silhouette coefficient for landmark l_i as

$$s_i = \frac{LF(b_i) - LF(a_i)}{\max \{LF(b_i), LF(a_i)\}}. \quad (8)$$

Since a value of s_i close to 1 means that l_i is appropriately clustered in Ω_i , the optimal clustering of S will be the one that maximizes the average s_i . Note that the resolution superscript r , was omitted in (8) for clarity. Figs. 3 and 4 show the landmark clusterization obtained at each resolution for two different cases, the subcortical structures of the brain and the set of abdominal organs, respectively.

5. Shape modeling via GEM-PDM

Once the hierarchical multi-resolution decomposition of the structure has been defined, GEM-PDM can be used to generate new instances of the objects of interest (i.e., fitting the model to a new set of points that identify the potential location of the structure in a new image). In this section, we describe a coarse-to-fine approach to model new shapes via GEM-PDM. The potential inconsistency in the border regions of adjacent patches is also addressed here. Finally, a step-by-step description of the shape modeling algorithm is presented.

5.1. Coarse-to-fine shape modeling

Let \mathbf{x} be the vector form of the multi-object structure under study, whose multi-resolution hierarchical decomposition (i.e., hierarchical landmark clusterization and statistical modeling) is obtained according to the procedures described in the previous sections. Suppose that now we want to use the new GEM-PDM to describe a new case, \mathbf{y} , i.e., finding the best approximation of \mathbf{y} in the subspace of allowed shapes described by the statistical model. Starting from the coarsest resolution ($r = R$), \mathbf{y}^r is divided into the M^r subsets defined in Section 4 (in particular, we impose the initial constraint $M^R = 1$), each being corrected by the corresponding PDM (5). The resulting constrained shape, \mathbf{x}^r is combined with the original wavelet information, \mathbf{z}^r , to create \mathbf{y}^{r-1} by means of the synthesis equation (3). This process is repeated at each resolution until $r = 0$. Because the corrections imposed at r via PDM can be altered at the subsequent resolution, $r - 1$, the above procedure is repeated iteratively until convergence or a maximum number of iterations is reached.

5.2. Inter-regions consistency

Along with its simplicity, another interesting property of PDM is the capacity to correct potential inaccuracies in the target shape, \mathbf{y} . In practice, \mathbf{y} is typically obtained by means of some image-based matching process (see Cootes et al. (1995) or van Ginneken et al. (2002) for details), which may contain significant inconsistencies due to the use of over-simplistic appearance models, and the presence of noise or artifacts in the image. The creation of new appearance models being able to adequately characterize the texture of the organs of interest is still a very active research field (Cheng et al., 2014; Islam et al., 2013; Rathore et al., 2011; Sukno et al., 2007; van Ginneken et al., 2002). Despite the possible inconsistency of the resulting shape, the legitimacy of the final form is guaranteed by the shape model, providing the best approximation of \mathbf{y} in the subspace of valid shapes.

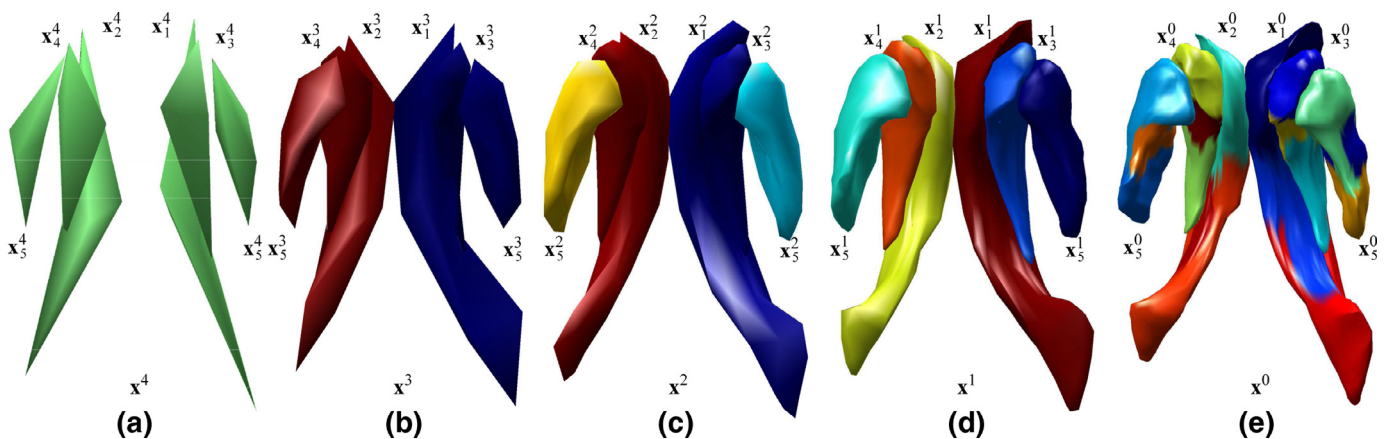


Fig. 3. Multi-resolution decomposition and hierarchical configuration provided by the GMRH-PDM algorithm for the multi-object structure composed by six subcortical structures of the brain. At each level of resolution, the set of landmarks depicted with the same color are modeled jointly via PDM. At resolution x^1 the lateral ventricles are in dark red (x_1^1) and yellow (x_2^1), the caudate nuclei in navy (x_3^1) and orange (x_4^1), and the putamens in dark blue (x_5^1) and cyan (x_6^1). (For interpretation of the references to color in this figure legend, the reader is referred to the web version of this article.)

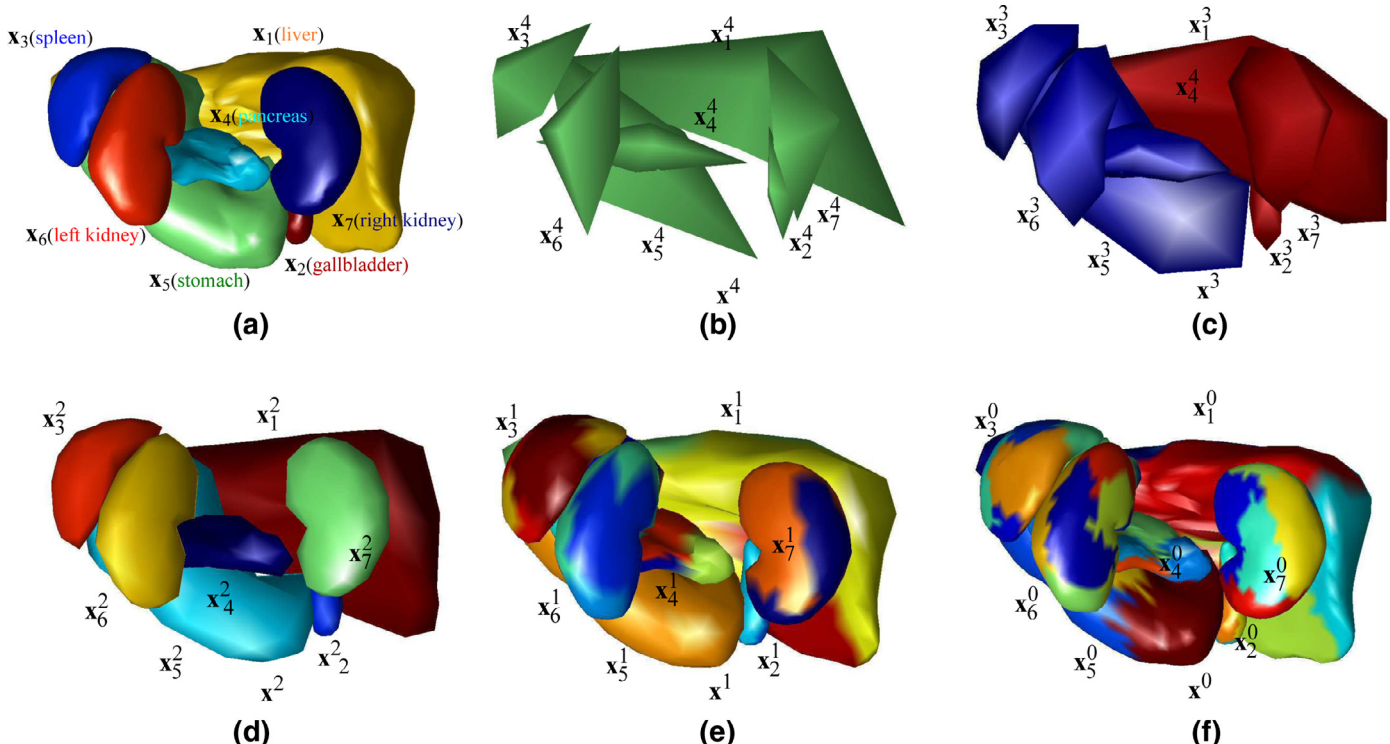


Fig. 4. Set of the abdominal structures considered in the study. (a) Identification of the seven structures under study. Each organ is depicted with a different color for representation purpose. (b)–(f) Multi-resolution decomposition and hierarchical configuration for the multi-object structure composed by seven abdominal structures. At each level of resolution, the set of landmarks depicted with the same color are modeled jointly via PDM. (For interpretation of the references to color in this figure legend, the reader is referred to the web version of this article.)

In GEM-PDM, relaxing the definition of the minimum unit than can be modeled independently allows us to model complex multi-object structures more efficiently than traditional PDMs. As a result of this new paradigm, an organ can be divided into multiple sub-parts as we move toward higher resolutions (see Figs. 2 and 3). Despite the fact that the coarse-to-fine multi-resolution modeling approach described in Section 5.1 guarantees the general consistency of the set, additional constraints may be necessary in the border regions between patches in order to prevent the overlapping and to preserve the relative position between landmarks. As it can be deduced from Section 5.1, the consistency between adjacent regions, \mathbf{S}_1^r and \mathbf{S}_2^r , is partially handled at coarser resolutions since $(\mathbf{S}_1^{r-1}, \mathbf{S}_2^{r-1}) \subseteq \widehat{\mathbf{S}}_1^r$. However, since no correction is performed on the wavelet term \mathbf{z}^r used

to estimate \mathbf{y}^{r-1} from \mathbf{x}^r , it can generate some residual overlapping inaccuracies (see Fig. 5(a) and (b)).

Given \mathbf{S}_s^r , we define the expansion of grade 1 of this region, $\check{\mathbf{S}}_{s,1}^r$, as the union of \mathbf{S}_s^r and those landmarks directly connected to the border of the region; i.e., those landmarks that belong to the same triangular face (assuming we use triangulated meshes to represent objects) than the border points of \mathbf{S}_s^r , but not included in it. Recursively, $\check{\mathbf{S}}_{s,2}^r$ can be defined as the expansion of grade 1 of $\check{\mathbf{S}}_{s,1}^r$, and so on (see Fig. 5(c)). This allows us to define overlapping areas when creating the statistical shape models for each region. The final location of those landmarks included in more than one region is defined as the average of the positions suggested by each expanded statistical model (i.e., $\text{PCA}(\check{\mathbf{S}}_{s,2}^r)$), weighted by the distance function e^{-D^2} , where D is the

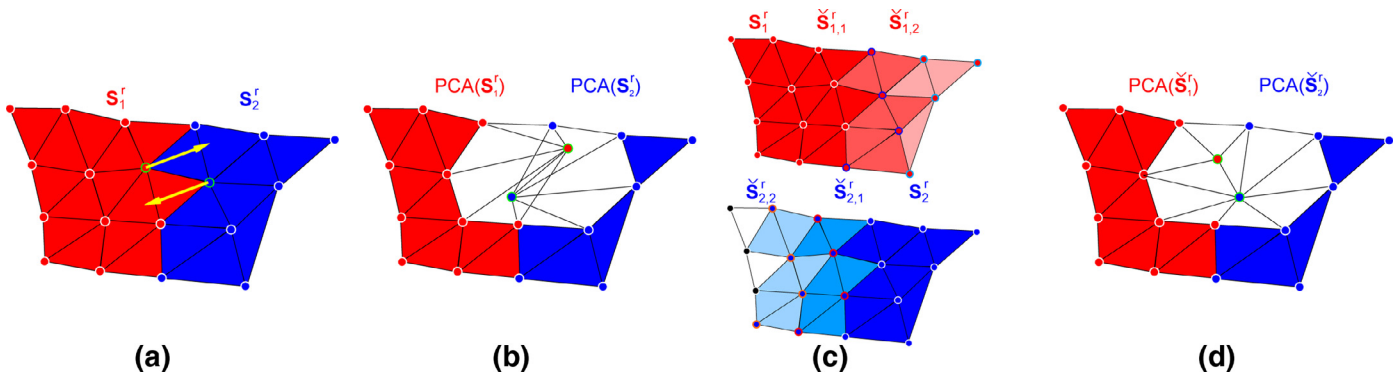


Fig. 5. Example of the inter-regions consistency preservation. (a) Example of two adjacent regions, S_1^r and S_2^r . The arrows show the new position of the two highlighted landmarks after the appearance model-based updating stage. (b) Inconsistency of the shape when using two independent shape models, $PCA(S_1^r)$ and $PCA(S_2^r)$. (c) Expansion of grade 1, and 2 ($\check{S}_{1,1}^r, \check{S}_{2,1}^r$), and 2 ($\check{S}_{1,2}^r, \check{S}_{2,2}^r$), of regions S_1^r and S_2^r . (d) New landmarks position using the weighted sum of the two expanded shape models (see Eq. (9)), i.e., $PCA(\check{S}_{1,2}^r)$ and $PCA(\check{S}_{2,2}^r)$.

geodesic distance (Mitchell et al., 1987) to the original non-expanded region, S_s^r (see Fig. 5(d)). Suppose landmark l belongs to the expanded regions $\check{S}_{1,2}^r$ and $\check{S}_{2,2}^r$, and that \check{l}_1 and \check{l}_2 are the new corrected positions for l proposed by the statistical shape models of $\check{S}_{1,2}^r$ and $\check{S}_{2,2}^r$, respectively. Thus, the final location for l is defined as

$$l = w_1\check{l}_1 + w_2\check{l}_2 = \frac{e^{-D_{l,1}^2}\check{l}_1 + e^{-D_{l,2}^2}\check{l}_2}{e^{-D_{l,1}^2} + e^{-D_{l,2}^2}}, \quad (9)$$

where $D_{l,1}$ and $D_{l,2}$ are the geodesic distance of l to the original S_1^r and S_2^r , respectively. In our experience, working with expansions of grade 1 or 2 is sufficient to guarantee satisfactory results.

5.3. Description of the algorithm

A step-by-step description of the new shape modeling algorithm is detailed in [Algorithm 1](#).

```

Input:  $\mathbf{y}$ ; \\ Target shape to model;
 $\mathbf{x}^0 = \mathbf{y}$ ; \\ Initialization;
while (not convergence) or (not max. iterations) do
     $\mathbf{x}^0 \longrightarrow \{\mathbf{x}^R, \mathbf{z}^R, \mathbf{z}^{R-1}, \dots, \mathbf{z}^1\}$ ; \\ Multi-resolution
    decomposition using (1) and (2);
    for  $r = R$  to 1 do
        for  $s = 1$  to  $M^r$  do
             $\tilde{\mathbf{x}}_{s,d}^r = \{\tilde{\mathbf{x}}^r(j) : j \in \check{S}_{s,d}^r\}$ ; \\ Build the expansion of
            grade  $d$  for each region ;
             $PDM_s^r(\tilde{\mathbf{x}}_{s,d}^r) = \hat{\mathbf{x}}_{s,d}^r$ ;
        end
         $\hat{\mathbf{x}}_{s,d}^r \longrightarrow \tilde{\mathbf{x}}_s^r$ ; \\ Solve overlapping between regions using
        geodesic distance;
         $\hat{\mathbf{x}}^r = \cup_{s=1}^{M^r} \hat{\mathbf{x}}_s^r$ ;
        if  $r > 0$  then
             $\tilde{\mathbf{x}}^{r-1} = \mathbf{F}^r \hat{\mathbf{x}}^r + \mathbf{G}^r \mathbf{z}^r$ ; \\ Shape resolution updating
            using (3);
        end
    end
     $\mathbf{x}^0 = \tilde{\mathbf{x}}^0$ ;
end

```

Algorithm 1: GEM-PDM.

6. Results

In this section we present a set of experiments to analyze and quantify the potential of the new hierarchical shape modeling frame-

work presented here to characterize the underlying population of a given set of training shapes and its ability to generate new valid instances. We also characterize the performance of the model in terms of robustness and its capacity to adequately correct invalid cases out of the subspace of allowed shapes. The behavior of GEM-PDM is compared with two alternative methods: the original PDM proposed by Cootes et al. (1995), and one of the most popular hierarchical variants presented by Davatzikos et al. (2003), the hierarchical PDM (HPDM). To evaluate the utility of GEM-PDM in the context of a real segmentation task, GEM-PDM is also compared with the two segmentation approaches based on PDM and HPDM, i.e., the classical ASM framework (Cootes et al., 1995; 1994), and the hierarchical ASM (HASM), respectively. Finally, we analyze the potential of GEM-PDM for the study of anatomical variability within organs, and its correlation with known anatomical deformations.

In our experiments, we use two different databases. First we use a set of 18 T1-weighted brain MRI volumes obtained from the Internet Brain Segmentation Repository (IBSR) (IBSR, 2006) (pixel resolution $0.94 \times 0.94 \times 1.5$ mm; volumes: $256 \times 256 \times 128$ voxels). In particular, we work with a multi-object configuration composed of six subcortical structures, including the left and right lateral ventricles, left and right caudate nuclei, and left and right putamens (see Fig. 1). We also use a proprietary database of 18 CT abdominal studies (pixel resolution: $0.58 \times 0.58 \times 1.00$ mm; volumes: $512 \times 512 \times 360$ voxels). In this case, the structure under study consists of 7 abdominal organs, including the liver, the gallbladder, the spleen, the pancreas, the stomach, and the left and right kidneys (see Fig. 3(a)). In both cases, the maximum resolution is defined by the lowest number of landmarks necessary to represent the shapes of interest with an average point-to-surface error lower than 0.01 mm. Thus, we define a multi-resolution domain with 5 levels, i.e., $R_S = 4$, using 1026 points to describe each organ at the finest resolution level. The dense point correspondence between all shapes of the training sets was established via mesh-to-mesh registration (Heimann and Meinzer, 2009). In particular, we use the shape context method proposed by Belongie et al. (2002), where regularized thin-plate splines are used to align two shapes based on the point correspondences obtained from the shape context descriptors (i.e., an expanded vector of features defined for each point).

6.1. Hierarchical configuration

In GEM-PDM there are three configuration parameters that control the clusterization process, α_1 , α_2 and α_3 (see (6)). Following the general guidelines described in [Section 4](#), α_1 , α_2 and α_3 , are set to 0.8, 0.1 and 0.1, respectively. Experimentally, we observed great similarity between the clusters obtained when $\alpha_1 \in [0.7, 0.9]$ with

Table 1

Subcortical brain structures – Shape modeling accuracy. ◊ marks statistically significant improvements over classic PDM; * marks statistically significant improvement over HPDM; ◊◊ marks statistically significant improvement over classic PDM and HPDM; (p -value < 0.05).

No noise added							
	LV	RV	LC	RC	LP	RP	Avg.
P2S (mm)							
PDM	0.99 ± 0.21	1.04 ± 0.32	0.66 ± 0.14	0.70 ± 0.14	0.66 ± 0.15	0.66 ± 0.11	0.78 ± 0.25
HPDM	0.90 ± 0.16	1.03 ± 0.32	0.74 ± 0.15	0.72 ± 0.15	0.71 ± 0.17	0.69 ± 0.12	0.80 ± 0.22
GEM-PDM	0.82 ± 0.19◊	0.81 ± 0.20◊	0.59 ± 0.09◊	0.68 ± 0.14◊	0.59 ± 0.09◊	0.59 ± 0.06◊	0.68 ± 0.17◊
DC							
PDM	0.81 ± 0.05	0.80 ± 0.05	0.87 ± 0.03	0.86 ± 0.03	0.89 ± 0.03	0.89 ± 0.02	0.85 ± 0.05
HPDM	0.82 ± 0.04	0.80 ± 0.05	0.85 ± 0.03	0.85 ± 0.03	0.88 ± 0.03	0.89 ± 0.02	0.85 ± 0.04
GEM-PDM	0.84 ± 0.05◊	0.84 ± 0.04◊	0.88 ± 0.02*	0.87 ± 0.03	0.90 ± 0.01	0.91 ± 0.01◊	0.87 ± 0.04◊
Noise 5 mm							
	LV	RV	LC	RC	LP	RP	Avg.
P2S (mm)							
PDM	1.00 ± 0.24	1.07 ± 0.33	0.67 ± 0.15	0.71 ± 0.15	0.67 ± 0.16	0.68 ± 0.11	0.80 ± 0.19
HPDM	1.90 ± 0.16	1.94 ± 0.35	1.36 ± 0.16	1.41 ± 0.10	1.35 ± 0.15	1.34 ± 0.11	1.55 ± 0.17
GEM-PDM	1.00 ± 0.18*	1.03 ± 0.25*	0.68 ± 0.13*	0.74 ± 0.13*	0.69 ± 0.15*	0.70 ± 0.15*	0.81 ± 0.16*
DC							
PDM	0.81 ± 0.05	0.80 ± 0.05	0.87 ± 0.03	0.86 ± 0.03	0.89 ± 0.03	0.89 ± 0.02	0.85 ± 0.04
HPDM	0.53 ± 0.08	0.52 ± 0.10	0.62 ± 0.05	0.59 ± 0.04	0.69 ± 0.05	0.70 ± 0.03	0.61 ± 0.06
GEM-PDM	0.81 ± 0.04*	0.80 ± 0.04*	0.86 ± 0.03*	0.85 ± 0.03*	0.89 ± 0.02*	0.89 ± 0.03*	0.85 ± 0.03*
Noise 15 mm							
	LV	RV	LC	RC	LP	RP	Avg.
P2S (mm)							
PDM	1.32 ± 0.07	1.43 ± 0.07	0.88 ± 0.04	0.99 ± 0.06	1.05 ± 0.03	1.00 ± 0.06	1.11 ± 0.0
HPDM	5.51 ± 0.06	5.15 ± 0.07	3.84 ± 0.03	3.89 ± 0.03	3.46 ± 0.03	3.38 ± 0.03	4.21 ± 0.04
GEM-PDM	1.18 ± 0.06◊	1.28 ± 0.04◊	0.73 ± 0.02◊	0.82 ± 0.03◊	0.73 ± 0.03◊	0.81 ± 0.03◊	0.92 ± 0.03◊
DC							
PDM	0.75 ± 0.30	0.74 ± 0.47	0.82 ± 0.19	0.81 ± 0.24	0.83 ± 0.30	0.84 ± 0.32	0.80 ± 0.30
HPDM	0.16 ± 0.67	0.16 ± 0.78	0.19 ± 0.46	0.19 ± 0.41	0.28 ± 0.28	0.29 ± 0.32	0.21 ± 0.49
GEM-PDM	0.77 ± 0.24*	0.74 ± 0.29*	0.85 ± 0.13◊	0.83 ± 0.12◊	0.88 ± 0.14◊	0.87 ± 0.17*	0.82 ± 0.18◊

$\alpha_2 = \alpha_3 = (1 - \alpha_1)/2$. For $\alpha_1 < 0.7$, the landmarks grouped into a single large cluster, as the second and third term of (6) control the clusterization process. For $\alpha_1 > 0.9$, the landmarks were over-clustered due to the under penalization of partitions. Imposing the initial constraint $M^R = 1$, the resulting configurations for both databases are shown in Figs. 2 and 3. In the case of the subcortical structures of the brain, the hierarchical configuration proposes the division of the organs into two groups at $r = 3$, coinciding with the left and right hemisphere of the brain. At $r = 2$, adjacent objects are modeled together, and at $r = 1$, each subcortical structure is considered independently. The subdivision of each organ into smaller subsets of landmarks at $r = 0$ can be observed in Fig. 2(e).

After modeling together the whole set of abdominal organs at the coarsest resolution, two groups were created at $r = 3$ for the left and right abdomen: spleen, stomach, pancreas and left kidney, and liver, gallbladder and right kidney, respectively. At $r = 2$ each organ was modeled independently. The subsets in which each organ is divided at finer resolutions are depicted in Fig. 3(e) and (f). The possible anatomical interpretation of some of these clusters is discussed in Section 6.4. It is interesting to note how the individual organs of interest in both databases were automatically clustered at $r = 1$ and $r = 2$ for the brain and the abdominal databases, respectively, incorporating the modeling of each organ in the multi-resolution hierarchical model.

Like most of the agglomerative clustering approaches, the complexity of the tailored version of Ward's algorithm (Ward, 1963) presented in Section 4 is $O(n^3)$. In particular, the computational cost of the hierarchical clustering was 100 min for both databases (implementations based on Matlab® R2014a 64-bits, using a 2.80 GHz Intel® Xeon® with 16GB of RAM). Finally, note that the hierarchical clustering process is a one-time offline process for each of the databases considered in the study.

6.2. Statistical shape modeling accuracy

The three statistical models under study, PDM, HPDM, and GEM-PDM, were built to explain 98% of the variability observed in the training set, restricting the deformation space around the mean shape to twice the standard deviation in each deformation vector (i.e., each eigenvector). The resulting number of eigenvectors was different for each statistical shape model. The accuracy of the three methods to model new instances of the underlying population was evaluated in terms of the symmetric point-to-surface distance (P2S) and Dice coefficient (DC), using leave-one-out cross-validation. In particular, three different sets of shapes were used to characterize the capacity of the models to generate new instances, as well as their robustness, on each database: the original ground-truth (i.e., shapes), and noisy shapes in which different levels of Gaussian noise were added to each axis: zero-mean normal random noise with standard deviation of 5 mm and 15 mm. The results obtained for the brain and the abdominal databases are shown in Tables 1 and 2, respectively. Significance was assessed using the Wilcoxon rank sum test and a p -value of 0.05.

When modeling images without noise added, it can be observed that the new GEM-PDM provides a significant improvement over the two alternative approaches, PDM and HPDM, for most of the subcortical brain structures, obtaining an average P2S distance of 0.68 ± 0.17 mm, and DC of 0.87 ± 0.04 (only the left putamen provided a p -value higher than 0.05). The significant advantage of GEM-PDM over PDM and HPDM was also validated for all the abdominal organs considered (average P2S distance of 3.35 ± 1.19 mm and DC of 0.80 ± 0.09), with the exception of the spleen, where both hierarchical approaches provided similar results.

The good performance of GEM-PDM is also appreciated when working with noisy shapes. In the case of the zero-mean normal noise

Table 2

Abdominal Structures – Shape modeling accuracy. ◊ marks statistically significant improvements over classic PDM; * marks statistically significant improvement over HPDM.; ◇ marks statistically significant improvement over classic PDM and HPDM; (p -value < 0.05).

No noise added								
	Spl.	Pan.	Liv.	LKid.	RKid.	Gall.	Stom.	Avg.
P2S (mm)								
PDM	5.60 ± 1.07	3.90 ± 1.33	4.68 ± 1.47	4.57 ± 1.65	5.96 ± 1.81	4.18 ± 1.50	4.50 ± 1.30	4.77 ± 1.59
HPDM	4.85 ± 1.19	4.02 ± 1.43	4.57 ± 1.32	4.28 ± 1.45	5.59 ± 1.82	4.18 ± 1.65	4.55 ± 1.31	4.58 ± 1.51
GEM-PDM	4.41 ± 0.66◊	2.74 ± 0.88◇	3.20 ± 1.30◊	3.49 ± 1.18◊	4.05 ± 1.14◊	3.18 ± 0.99◊	2.36 ± 0.80◊	3.35 ± 1.19◊
DC								
PDM	0.83 ± 0.04	0.63 ± 0.14	0.73 ± 0.08	0.60 ± 0.13	0.74 ± 0.06	0.78 ± 0.07	0.76 ± 0.07	0.72 ± 0.12
HPDM	0.86 ± 0.03	0.62 ± 0.15	0.74 ± 0.08	0.61 ± 0.12	0.76 ± 0.06	0.78 ± 0.08	0.76 ± 0.07	0.73 ± 0.12
GEM-PDM	0.86 ± 0.02◊	0.74 ± 0.09◊	0.82 ± 0.08◊	0.69 ± 0.10◊	0.82 ± 0.04◊	0.83 ± 0.05◊	0.87 ± 0.04◊	0.80 ± 0.09◊
Noise 5 mm								
	Spl.	Pan.	Liv.	LKid.	RKid.	Gall.	Stom.	Avg.
P2S (mm)								
PDM	4.70 ± 1.45	4.62 ± 1.63	5.60 ± 1.11	4.37 ± 1.52	4.58 ± 1.33	3.84 ± 1.32	5.95 ± 1.83	4.81 ± 1.46
HPDM	4.43 ± 1.27	4.17 ± 1.18	5.73 ± 0.79	4.31 ± 1.48	4.56 ± 1.27	3.49 ± 1.15	5.61 ± 1.67	4.61 ± 1.26
GEM-PDM	4.32 ± 1.46◊	4.42 ± 1.46*	5.20 ± 0.99◊	4.12 ± 1.43	4.31 ± 1.32*	3.85 ± 1.28*	5.46 ± 1.75◊	4.53 ± 1.38◊
DC								
PDM	0.73 ± 0.08	0.59 ± 0.13	0.82 ± 0.04	0.77 ± 0.08	0.75 ± 0.07	0.63 ± 0.13	0.73 ± 0.06	0.72 ± 0.08
HPDM	0.72 ± 0.07	0.59 ± 0.11	0.82 ± 0.02	0.76 ± 0.08	0.73 ± 0.07	0.61 ± 0.14	0.73 ± 0.07	0.71 ± 0.08
GEM-PDM	0.75 ± 0.08*	0.62 ± 0.12	0.84 ± 0.04◊	0.77 ± 0.07	0.77 ± 0.07*	0.64 ± 0.13*	0.76 ± 0.05◊	0.74 ± 0.08◊
Noise 15 mm								
	Spl.	Pan.	Liv.	LKid.	RKid.	Gall.	Stom.	Avg.
P2S (mm)								
PDM	5.16 ± 1.52	4.72 ± 1.63	5.82 ± 1.04	4.30 ± 1.45	4.78 ± 4.21	4.12 ± 1.37	6.14 ± 1.70	5.00 ± 1.42
HPDM	5.11 ± 1.03	4.45 ± 1.13	7.55 ± 0.90	4.69 ± 1.01	4.95 ± 0.93	4.08 ± 0.67	6.62 ± 1.42	5.35 ± 1.01
GEM-PDM	4.40 ± 1.41◊	4.41 ± 1.46◊	5.32 ± 1.02◊	4.17 ± 1.45	4.43 ± 1.39◊	3.80 ± 1.23◊	5.56 ± 1.79◊	4.58 ± 1.39◊
DC								
PDM	0.70 ± 0.08	0.57 ± 0.13	0.82 ± 0.04	0.76 ± 0.08	0.74 ± 0.07	0.61 ± 0.14	0.73 ± 0.07	0.70 ± 0.09
HPDM	0.60 ± 0.06	0.46 ± 0.09	0.69 ± 0.04	0.66 ± 0.08	0.64 ± 0.07	0.46 ± 0.11	0.62 ± 0.10	0.59 ± 0.08
GEM-PDM	0.77 ± 0.08◊	0.60 ± 0.12*	0.84 ± 0.04◊	0.78 ± 0.07*	0.76 ± 0.07◊	0.64 ± 0.13◊	0.76 ± 0.06*	0.74 ± 0.08◊

with 5 mm of standard deviation, both GEM-PDM (P2S: 0.81 ± 0.16 mm; DC: 0.85 ± 0.03) and PDM (P2S: 0.80 ± 0.19 mm; DC: 0.85 ± 0.04) provide similar results for the brain database, and both significantly outperform HPDM (P2S: 1.55 ± 0.17 mm; DC: 0.61 ± 0.06). For the abdominal structures GEM-PDM (P2S: 4.53 ± 1.38 mm, DC: 0.74 ± 0.08) provided significantly better results than the two alternative methods. In both databases, the performance of GEM-PDM was significantly better than the two alternatives approaches for a noise level of 15 mm.

As Cerrolaza et al. (2012) point out, the independent modeling of the bands used in HPDM significantly reduces the robustness of the model to noise, being especially sensitive to noisy cases. On the other hand, the classical approach of PDM tends to over-restrict the subspace of allowed shapes as a consequence of the HDLSS problem. While this provides significant modeling robustness to noise by ensuring that only valid shapes are generated even when dealing with noisy data, it also restricts the capability of the model to generate new instances. Thanks to the coarse-to-fine multi-resolution approach, and the overlapping between adjacent regions defined in Section 5.2, GEM-PDM is able to accurately model new instances of the underlying population, while equally guaranteeing the consistency of the final shape.

It is interesting to note that in general, all methods provided a greater shape modeling error for the abdominal cases than for the brain structures. While the number of training samples was the same in both cases, a higher variability, not only in the organ shape, but also in the spatial relations between them, was observed in the abdominal database, i.e., the HDLSS effect becomes more relevant. Despite the limited number of samples available, it can be observed that the new GEM-PDM outperformed the two alternative methods considered, PDM and HPDM. Finally, note that the P2S distance can be also

increased by the larger size of the organs involved in the abdominal database.

6.3. Segmentation of 3D brain MRI

In this section, we analyze the integration of the new GEM-PDM into a segmentation framework. In particular, our example addresses the segmentation of subcortical brain structures from MRI, one of the first applications of the original hierarchical model presented by Cerrolaza et al. (2012). In this paper, the segmentation was limited to 2D structures and the hierarchical configuration was defined manually. In this paper, we address the segmentation of 3D brain structures, a more interesting and challenging scenario, where to overcome the inherent limitations of the original formulation by GEM-PDM (i.e., the difficulty of manually defining the hierarchical configuration that provides optimal performance, and the constraint of modeling entire objects at the finest resolution) becomes essential. Moreover, the new GEM-PDM can additionally model sub-organ structures, which was not possible in the original framework. The performance of the resulting GEneralized Multi-resolution Active shape model shape model (GEMA), is compared with the two segmentation approaches based on PDM and HPDM, i.e., the classical ASM framework (Cootes et al., 1995; 1994), and the hierarchical ASM (HASM), respectively. To guide the matching process to a new image, we used one of the classical search profile appearance models frequently used in the context of ASM (Cootes et al., 1995; 1994), defined by the mean and the covariance matrix of the normalized first derivative of fixed-size gray profiles, normal to the boundary and centered at each landmark. The length of these profiles was set to 5 voxels, defining a search space of 9 pixels. The initialization was obtained by means of 3D rigid image registration between a reference image from the training set and

Table 3

Subcortical brain structures – Segmentation accuracy. * marks statistically significant improvement over HPDM.; \odot marks statistically significant improvement over classic PDM and HPDM; (p -value < 0.05).

	No noise added						
	LV	RV	LC	RC	LP	RP	Avg.
P2S (mm)							
PDM	1.35 ± 0.63	1.50 ± 0.69	0.77 ± 0.21	0.83 ± 0.21	0.73 ± 0.17	0.76 ± 0.11	0.99 ± 0.33
HPDM	1.64 ± 0.39	1.73 ± 0.47	1.33 ± 0.36	1.24 ± 0.33	1.46 ± 0.56	1.52 ± 0.47	1.49 ± 0.43
GEM-PDM	$0.99 \pm 0.19 \odot$	$1.07 \pm 0.30 \odot$	$0.71 \pm 0.15^*$	$0.77 \pm 0.17^*$	$0.72 \pm 0.16^*$	$0.73 \pm 0.07^*$	$0.83 \pm 0.17 \odot$
DC							
PDM	0.76 ± 0.12	0.73 ± 0.13	0.85 ± 0.05	0.84 ± 0.04	0.88 ± 0.03	0.88 ± 0.02	0.82 ± 0.07
HPDM	0.64 ± 0.09	0.62 ± 0.10	0.68 ± 0.09	0.71 ± 0.08	0.72 ± 0.10	0.73 ± 0.08	0.68 ± 0.09
GEM-PDM	$0.82 \pm 0.05 \odot$	$0.81 \pm 0.05 \odot$	$0.86 \pm 0.03^*$	$0.85 \pm 0.03^*$	$0.88 \pm 0.02^*$	$0.88 \pm 0.01^*$	$0.85 \pm 0.03 \odot$

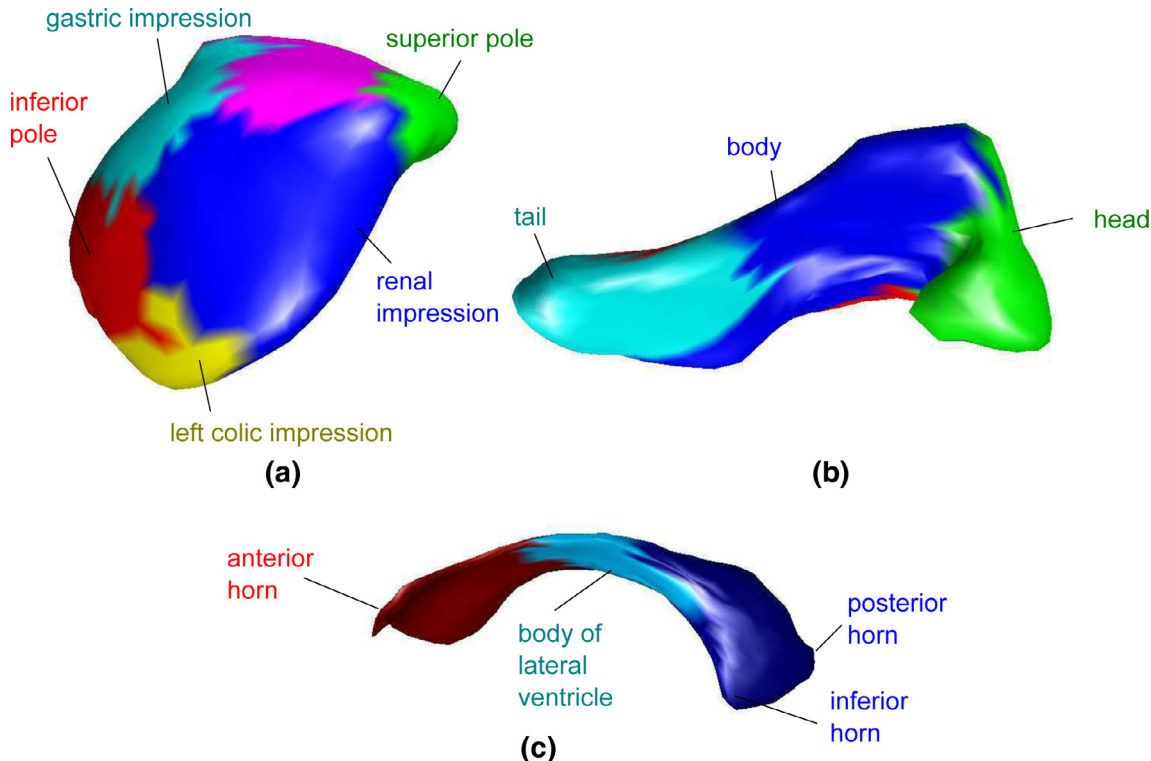


Fig. 6. Clusterization results of the spleen (a), the pancreas (b), and the left lateral ventricle (c) at the finest level of resolution used in this paper, and their qualitative relations to anatomical sections of the organs.

the target image, using the sum of squared differences as similarity measure (Crum et al., 2004; Myronenko, 2010). The resulting deformation field was used to obtain the initial estimation of the shape. All parameters were identical between the compared methods: ASM, HASM and GEMA, respectively.

Table 3 shows the accuracy of the three tested algorithms in terms of P2S and DC, using the leave-one-out cross-validation. It can be observed how the new segmentation algorithm, GEMA (avg.P2S: 0.83 ± 0.17 mm; avg.DC: 0.85 ± 0.03), provided a significantly better overall performance in terms of both P2S and DC than the other two algorithms, ASM (avg.P2S: 0.99 ± 0.33 mm; avg.DC: 0.82 ± 0.07), and HASM (avg.P2S: 1.49 ± 0.43 mm; avg.DC: 0.68 ± 0.09). Even more, compared to the 2D case considered in Cerrolaza et al. (2012), GEMA provides better accuracy than the best manual configuration proposed there (DC: 0.81 ± 0.07). It can be appreciated how the segmentations obtained with ASM and GEMA were generally better than the ones provided by HASM. As discussed in Cerrolaza et al. (2012), HASM is inefficient when dealing with the noisy shapes generated during the image-based matching process of a real segmentation process.

Finally, note that the computational cost of the hierarchical approaches, GEMA (~5 min.), and HASM (~7 min.), is slightly higher than the cost of the classical ASM (~3 min.), due to the additional operations associated with the wavelet-based multi-resolution decomposition (all implementations were in Matlab® R2014a 64-bits, using a 2.80 GHz Intel® Xeon® with 16GB of RAM).

6.4. Anatomical variability of organs

Another interesting application of the hierarchical decomposition introduced in Section 4 is the study of anatomical variability of organs, and of inter-organs relations. According to the original works presented by Reyes et al. (2010); 2009, the analysis of deformation fields showed correlation with existing anatomical landmarks and known anatomical deformations of abdominal organs. The subdivision of organs into anatomically significant components defined by clusters may be of great utility in the study and analysis of the anatomical variability of organs and inter-organs relations, an important research tool for diagnosis, modeling, and soft tissue intervention. In particular, Reyes et al. focused their interest in the study of

abdominal structures, though from a single-organ or local perspective. Here, the new general landmark clustering framework introduced in [Section 4](#) allows us to address the problem from a more global perspective. Thanks to the energy minimization process defined by [Eqs. \(6\)](#) and [\(8\)](#), the clusterization process allows us to identify those groups of landmarks with similar anatomical and mechanical characteristics (e.g., similar deformation fields, or spatial proximity). Thus, as it was discussed in [Section 6.1](#), broader inter-organ relations are considered at coarser resolutions, creating smaller groups as we move toward finer resolutions (see [Fig. 3](#)). For instance, it is possible to appreciate how the two groups created at $r = 3$ are composed of organs with known anatomical relations between them, such as the liver, gallbladder and right kidney, or the left kidney, spleen and pancreas ([Fig. 4\(c\)](#)). These organ relations or correlations were also observed by [Okada et al. \(2013\)](#).

In [Fig. 6](#) we go one step further and show how it is possible to establish a direct relation between the clusters obtained at finest resolutions, and known anatomical and functional sections of the organs. At this stage of our work, these intra-organ clusters were evaluated qualitatively by an expert radiologist. The intra-organ analysis is not a focus of this manuscript and these preliminary results are shown for exemplification only.

[Fig. 6\(a\)](#) shows the correspondence between the clusters of the spleen with the superior and inferior poles, and the renal, gastric, and left colic impressions. [Fig. 6\(b\)](#) identifies the three parts in which the pancreas can be divided, the head, the body and the tail. [Fig. 6\(c\)](#) shows how the clusterization process divides the left lateral ventricle into three different regions, which can be identified with the anterior horn, the body, and the posterior and inferior horn. It can be observed how the posterior and inferior horns of the left lateral ventricle are included within the same clusters, in spite of being two different anatomical regions. A possible explanation is the absence of the posterior horn in many instances. The posterior horns are very thin structures barely detectable in MRI, due to partial volume effects ([Rajamani et al., 2007](#)). As a consequence, the manual segmentations provided by the IBSR database are not always consistent, and the posterior horn is missing in many cases. This issue suggests an interesting possible extension of our framework: the multi-structure methodology could be adapted to deal with missing structures.

7. Discussion and conclusions

In this paper, we presented a general multi-resolution framework for the statistical modeling of multi-object structures. Unlike the classical single-object modeling approach of PDM, the new GEM-PDM creates different statistical shape models that characterize specific inter-organs associations at each level of resolution. The goal of this strategy is twofold: to reduce the HDLSS challenge, particularly relevant in new medical imaging applications, where the number of training images is often small, and to efficiently capture the interaction between adjacent regions, in addition to the shape variation of individual organs. This GEM-PDM also tackles the two main drawbacks observed in previous hierarchical approaches: the difficulty of manually defining the hierarchical configuration that provides optimal performance, and the limitation of considering the single objects as the simplest structure to model. Relaxing this latter condition, we go one step further in the development of hierarchical PDMs, presenting a general framework where any possible grouping of landmarks is considered. Finally, the hierarchical configuration of the algorithm is completely automated thanks to the new agglomerative landmark clustering approach, whose optimization is controlled by a tailored definition of the Silhouette coefficient.

The performance of GEM-PDM was evaluated in terms of shape modeling accuracy and noise robustness, and compared with two popular alternatives: the classical PDM and HPDM. The results show how the new general framework significantly outperformed both al-

ternative approaches for two different tested databases: the set of six brain subcortical structures and the set of seven abdominal organs.

Finally, the new shape modeling framework was integrated into a real segmentation algorithm, GEMA, providing a better overall performance than the other two algorithms tested, ASM and HASM, when applied to the segmentation of subcortical structures.

In the near future, we will continue exploring the capability of GEM-PDM to automatically model comprehensive anatomical structures, from the multi-organ level to the inter- and intra-object resolution, and formalize the anatomic and functional relations between organs, which can be of great interest in the context of full body computational anatomy.

Acknowledgments

This project was supported in part by a philanthropic gift from the Government of Abu Dhabi to Children's National Health System, and by the European Union FP7 project HEAR-EU (grant agreement 304857). We also like to thank the Intramural Research Program of the National Institute of Health, Clinical Center.

References

- Belongie, S., Malik, J., Puzicha, J., 2002. Shape matching and object recognition using shape contexts. *IEEE Trans. Pattern Anal. Mach. Intell.* 24 (4), 509–522.
- Cerrolaza, J., Villanueva, A., Cabeza, R., 2012. Hierarchical statistical shape models of multiobject anatomical structures: application to brain MRI. *IEEE Trans. Med. Imaging* 31 (3), 713–724. doi:10.1109/TMI.2011.2175940.
- Cerrolaza, J., Villanueva, A., Reyes, M., Cabeza, R., Gonzalez Ballester, M., Linguraru, M., 2014. Generalized multiresolution hierarchical shape models via automatic landmark clusterization. In: Golland, P., Hata, N., Barillot, C., Hornegger, J., Howe, R. (Eds.), *Medical Image Computing and Computer-Assisted Intervention – MICCAI 2014*. In: Lecture Notes in Computer Science, 8675. Springer International Publishing, pp. 1–8. doi:10.1007/978-3-319-10443-0_1.
- Cheng, K., Montgomery, D., Yang, F., McLaren, D.B., McLaughlin, S., Nailon, W.H., 2014. Active shape models with optimised texture features for radiotherapy. In: Proc. SPIE, pp. 90362G-1–90362G-5.
- Cootes, T., Taylor, C., Cooper, D., Graham, J., 1995. Active shape models-their training and application. *Comput. Vis. Image Understand.* 61 (1), 38–59.
- Cootes, T.F., Taylor, C., Lanitis, A., 1994. Active shape models: evaluation of a multi-resolution method for improving image search. In: *Proceedings of the British Machine Vision Conference*, vol. 5, pp. 327–336.
- Crum, W., Hartkens, T., Hill, D., 2004. Non-rigid image registration: theory and practice. *Brit. J. Radiol.* 77 (SPEC. ISS. 2), S140–S153.
- Davatzikos, C., Tao, X., Shen, D., 2003. Hierarchical active shape models, using the wavelet transform. *IEEE Trans. Med. Imaging* 22 (3), 414–423.
- Duta, N., Sonka, M., 1998. Segmentation and interpretation of mr brain images. an improved active shape model. *IEEE Trans. Med. Imaging* 17 (6), 1049–1062. doi:10.1109/42.746716.
- Finkelstein, A., Salesin, D.H., 1994. Multiresolution curves. In: *Proceedings of the 21st Annual Conference on Computer Graphics and Interactive Techniques*. ACM, New York, NY, USA, pp. 261–268. doi:10.1145/192161.192223.
- González-Ballester, M.Á., Zisserman, A.P., Brady, M., 2002. Estimation of the partial volume effect in [MRI]. *Med. Image Anal.* 6 (4), 389–405.
- Grenander, U., Chow, Y., Keenan, D.M., 1991. *Hands: A Pattern Theoretic Study of Biological Shapes*. Springer-Verlag New York, Inc., New York, NY, USA.
- Hamarneh, G., Gustavsson, T., 2004. Deformable spatio-temporal shape models: extending active shape models to 2d+time. *Image Vis. Comput.* 22 (6), 461–470.
- Heimann, T., Meinzer, H.-P., 2009. Statistical shape models for 3D medical image segmentation: A review. *Med. Image Anal.* 13 (4), 543–563.
- IBSR, 2006. The internet brain segmentation repository (IBSR). Available from <http://www.cma.mgh.harvard.edu/ibsr/>.
- Islam, A., Reza, S., Iftekharuddin, K., 2013. Multifractal texture estimation for detection and segmentation of brain tumors. *IEEE Trans. Biomed. Eng.* 60 (11), 3204–3215.
- Kelemen, A., Szekely, G., Gerig, G., 1998. Three-dimensional model-based segmentation of brain MRI. In: *Proceedings Workshop on Biomedical Image Analysis*, 1998, pp. 4–13. doi:10.1109/BIA.1998.692374.
- Linguraru, M.G., Pura, J.A., Pamulapati, V., Summers, R.M., 2012. Statistical 4D graphs for multi-organ abdominal segmentation from multiphase CT. *Med. Image Anal.* 16 (4), 904–914.
- Lounsbury, M., DeRose, T.D., Warren, J., 1997. Multiresolution analysis for surfaces of arbitrary topological type. *ACM Trans. Graph.* 16 (1), 34–73. doi:10.1145/237748.237750.
- Lu, C., Pizer, S., Joshi, S., Jeong, J.-Y., 2007. Statistical multi-object shape models. *Intl. J. Comput. Vis.* 75 (3), 387–404. doi:10.1007/s11263-007-0045-0.
- Mitchell, J.S.B., Mount, D.M., Papadimitriou, C.H., 1987. The discrete geodesic problem. *SIAM J. Comput.* 16 (4), 647–668.
- Myronenko, A., 2010. Technical Report.(Available from <https://sites.google.com/site/myronenko/research/mirt>)

- Okada, T., Linguraru, M., Hori, M., Summers, R., Tomiyama, N., Sato, Y., 2013. Abdominal multi-organ ct segmentation using organ correlation graph and prediction-based shape and location priors. In: Mori, K., Sakuma, I., Sato, Y., Barillot, C., Navab, N. (Eds.), *Medical Image Computing and Computer-Assisted Intervention – MICCAI 2013*. In: Lecture Notes in Computer Science, vol. 8151. Springer Berlin Heidelberg, pp. 275–282. doi:[10.1007/978-3-642-40760-4_35](https://doi.org/10.1007/978-3-642-40760-4_35).
- Okada, T., Yokota, K., Hori, M., Nakamoto, M., Nakamura, H., Sato, Y., 2008. Construction of hierarchical multi-organ statistical atlases and their application to multi-organ segmentation from CT images.. In: Metaxas, D.N., Axel, L., Fichtinger, G., Székely, G. (Eds.), *MICCAI* (1), vol. 5241. Springer, pp. 502–509.
- Praun, E., Hoppe, H., 2003. Spherical parametrization and remeshing. *ACM Trans. Graph.* 22 (3), 340–349. doi:[10.1145/882262.882274](https://doi.org/10.1145/882262.882274).
- Rajamani, K.T., Styner, M.A., Talib, H., Zheng, G., Nolte, L.-P., Ballester, M.A.G., 2007. Statistical deformable bone models for robust 3D surface extrapolation from sparse data.. *Med. Image Anal.* 11 (2), 99–109.
- Rao, A., Schunck, B., 1989. Computing oriented texture fields. In: *CVPR*, pp. 61–68.
- Rathore, S., Iftikhar, M., Hussain, M., Jalil, A., 2011. Texture analysis for liver segmentation and classification: a survey. In: *Frontiers of Information Technology (FIT)*, 2011, pp. 121–126.
- Reyes, M., González Ballester, M.A., Kozic, N., Summers, R.M., Linguraru, M.G., 2010. Hierarchical patch generation for multilevel statistical shape analysis by principal factor analysis decomposition. In: *Proc. SPIE*, pp. 762617-1–762617-8.
- Reyes, M., Gonzalez Ballester, M.A., Li, Z., Kozic, N., Chin, S., Summers, R., Linguraru, M., 2009. Anatomical variability of organs via principal factor analysis from the construction of an abdominal probabilistic atlas. In: *Biomedical Imaging: From Nano to Macro*, 2009. ISBI '09. IEEE International Symposium on, pp. 682–685. doi:[10.1109/ISBI.2009.5193139](https://doi.org/10.1109/ISBI.2009.5193139).
- Rockafellar, R.T., Wets, R.J.-B., 2005. *Variational Analysis*. Springer-Verlag New York, Inc., New York, NY, USA.
- Rousseeuw, P.J., 1987. Silhouettes: a graphical aid to the interpretation and validation of cluster analysis. *Comput. Appl. Math.* 20 (1), 53–65.
- Roy, T., Debreuve, E., Barlaud, M., Aubert, G., 2006. Segmentation of a vector field: dominant parameter and shape optimization. *J. Math. Imaging Vis.* 24 (2), 259–276. doi:[10.1007/s10851-005-3627-x](https://doi.org/10.1007/s10851-005-3627-x).
- Schroder, P., Sweldens, W., 1995. Spherical wavelets: texture processing. In: Hanrahan, P., Purgathofer, W. (Eds.), *Rendering Techniques '95*. Springer, Vienna. Eurographics, pp. 252–263. doi:[10.1007/978-3-7091-9430-0_24](https://doi.org/10.1007/978-3-7091-9430-0_24).
- Stollnitz, E.J., Derose, T.D., Salesin, D.H., 1996. *Wavelets for Computer Graphics: Theory and Applications*. Morgan Kaufmann Publishers Inc., San Francisco, CA, USA.
- Sukno, F., Ordas, S., Butakoff, C., Cruz, S., Frangi, A., 2007. Active shape models with invariant optimal features: application to facial analysis. *IEEE Trans. Pattern Anal. Mach. Intell.* 29 (7), 1105–1117.
- Suzuki, M., Linguraru, M., Okada, K., 2012. Multi-organ segmentation with missing organs in abdominal CT images. In: Ayache, N., Delingette, H., Golland, P., Mori, K. (Eds.), *Medical Image Computing and Computer-Assisted Intervention – MICCAI 2012*. In: Lecture Notes in Computer Science, vol. 7512. Springer, Berlin Heidelberg, pp. 418–425. doi:[10.1007/978-3-642-33454-2_52](https://doi.org/10.1007/978-3-642-33454-2_52).
- van Ginneken, B., Frangi, A., Staal, J., ter Haar Romeny, B., Viergever, M., 2002. Active shape model segmentation with optimal features. *IEEE Trans. Med. Imaging* 21 (8), 924–933. doi:[10.1109/TMI.2002.803121](https://doi.org/10.1109/TMI.2002.803121).
- Ward, J.H., 1963. Hierarchical grouping to optimize an objective function. *J. Am. Stat. Associat.* 58 (301), 236–244.